Super-Resolved Fine Scale Sea Ice Motion Tracking

Yang Xian, *Student Member, IEEE,* Zisis I. Petrou, *Member, IEEE,* Yingli Tian*, *Senior Member, IEEE,* and Walter N. Meier

***Abstract*—Monitoring sea ice activities is particularly critical to safe naval operations in the Arctic Ocean. Accurately tracking sea ice motions is essential to validate or even improve sea ice models for ice hazard forecasts at a fine scale. Fine-scale motions can be tracked from high-resolution radar or optical satellite imagery but with limited coverage. Daily motions over the entire Arctic are retrievable from passive microwave data, but at a much lower spatial resolution. Thus, providing motions at the passive microwave spatial and temporal coverage, but at an enhanced spatial resolution, will be a significant benefit. To break the resolution limitation and to boost tracking accuracy, a sequential super-resolved fine scale sea ice motion tracking framework is proposed in which a hybrid example-based single image super-resolution algorithm is employed before the tracking procedure. Experiments demonstrate that the proposed framework significantly improves the tracking performance in both accuracy and robustness for a benchmark algorithm and a recently proposed state-of-the-art tracking algorithm.**

***Index Terms*—AMSR2, example-based learning, maximum cross correlation, motion tracking, passive microwave, patch redundancy, sea ice, super-resolution, Suomi NPP.**

I. Introduction

Sea ice is a vital component in the Earth's climate as well as posing potential hazards to shipping and other maritime activities in the Polar regions. It is particularly critical to monitor and track the motions of sea ice in near real-time (i.e., within several hours of data acquisition) for safe naval operations in the Arctic Ocean, as well as to further validate or improve models of the polar ice pack, coupled with predictors like ocean temperatures, sea level pressure, and geostrophic winds, for ice hazard forecasts at a finer scale [1]–[4]. Several international operational ice centers provide routine tactical and strategic ice analyses in support of navigation and other activities in the Arctic, including the U.S. National Ice Center in Suitland, Maryland, USA [5].

The majority of operational sea ice monitoring techniques relies on satellite-borne optical and synthetic aperture radar (SAR) sensors, augmented by scatterometer and passive microwave imagery [6], [7]. Feasibility and accuracy in ice motion tracking hinge on the spatial and temporal resolutions of the input data. High spatial resolution (i.e., $100-1,000$ m) is possible with visible and SAR imagery, but at the cost of limited temporal sampling due to clouds (for visible imagery) or limited coverage (for SAR−narrow swaths, longer orbital repeat visits). On the other hand, passive microwave data can provide near-complete daily coverage over the entire Arctic, but at low spatial resolutions (i.e., $12.5-25$ km) [2], [8], [9].

Compared with other means of measuring ice drift (e.g., buoys), satellite sensors provide a more complete and routine coverage of Polar regions [10]. In particular, with the capabilities to penetrate cloud cover and observe the surface all day, satellite microwave sensors, including passive microwave sensors, are often considered as the best option to estimate sea ice drifts. The Defense Meteorological Satellite Program (DMSP) Special Sensor Microwave Radiometer and its predecessors, the Nimbus-7 Scanning Multichannel Microwave Radiometer (SMMR) and a series of DMSP Special Sensor Microwave/Imager (SSM/I) and Special Sensor Microwave Imager and Sounder (SSMIS) instruments have been operated for over 30 years, providing a long time-series of sea ice motion data [11].

Beginning in 2002, the National Aeronautics and Space Administration (NASA) Earth Observing System (EOS) Advanced Microwave Scanning Radiometer (AMSR-E) on the Aqua platform and the Japan Aerospace Exploration Agency (JAXA) AMSR2 sensor on the Global Change Observation Mission−Water (GCOM-W) platform have provided higher resolution passive microwave imagery. The higher spatial resolution (i.e., $5-12.5$ km) yields more accurate estimates of sea ice motions [12], [13], though fine scale motions (such as fractures and small lead openings) are still not detectable. These fine scale motions are important for effectively tracking energy fluxes, ice growth, and ocean freshwater fluxes. Moreover, they are critically important for navigational guidance in ice-infested waters. Providing motions at the passive microwave spatial and temporal coverage but at enhanced resolution will be a significant benefit.

This paper presents a test case application of image super-resolution (SR) method enhancing passive microwave derived sea ice motions. SR techniques have been utilized in the remote sensing field for various applications [14]–[16]. In this paper, we aim to accurately track sea ice motion at fine scales by first constructing high-resolution images with a hybrid example-based SR algorithm. Afterwards, a benchmark tracking algorithm based on maximum cross-correlation (MCC) [17] is applied to estimate sea ice drift vectors and track the sea ice movements. To our best knowledge, the proposed framework is the first to apply a hybrid example-based SR scheme for the sea ice tracking purpose. We adopt

Manuscript received Apr. 25, 2016, revised Aug. 15, 2016, accepted Apr. 2, 2017. This work was supported in part by ONR grant N000141310450.

Y. Xian is with the Department of Computer Science, The Graduate Center, The City University of New York, New York, NY, 10016 USA e-mail: yxian@gradcenter.cuny.edu.

Z. I. Petrou is with the Department of Electrical Engineering, The City College, The City University of New York, New York, NY, 10031 USA e-mail: zpetrou@ccny.cuny.edu.

Y. Tian is with the Department of Electrical Engineering, The City College and the Department of Computer Science, The Graduate Center, The City University of New York, New York, NY, 10031 USA phone: 212-650-7046; fax: 212-650-8249; e-mail: ytian@ccny.cuny.edu.

W. Meier is with Code 615, Cryospheric Science Lab, NASA Goddard Space Flight Center, Greenbelt, MD, 20771 USA e-mail: walt.meier@nasa.gov.

*Corresponding author.

the benchmark MCC algorithm since in principle, it can work on any type of imagery and has been successfully applied to sea ice with visible/infrared, scatterometer, SAR, and passive microwave data. To demonstrate the potential of the SR algorithm in further relevant applications, tracking of specific individual sea ice objects is additionally demonstrated using a state-of-the-art object tracking algorithm [18]. Overall, this paper shows that by using the super-resolved images, the accuracy of sea ice drift estimation is significantly improved compared to using the original images.

The rest of the paper is organized as follows: Section II introduces general background of SR and motion tracking methods. Section III describes the data used throughout this study. Section IV provides a detailed description of the proposed super-resolved sea ice motion tracking framework. Section V presents the experimental results and discussions. The conclusions are drawn in Section VI.

II. Related Work

A. Image Super-Resolution

Image SR aims to estimate a fine-resolution image from one or multiple coarse-resolution images. It has been successfully utilized in numerous applications such as medical imaging, video surveillance, desktop publishing, remote sensing, etc. Broadly speaking, depending on the number of input(s), image SR can be divided into two categories: multi-image SR [19]–[22] and single-image SR [23]–[34]. To alleviate the inherent ambiguity, single image SR generally relies on additional assumptions or priors to finalize a satisfying output.

Single image SR methods can be further classified as interpolation-based, reconstruction-based, and example learning-based depending on the upscaling scheme. Provided a low-resolution image, interpolation-based methods hinge on pre-defined mathematical formula to predict intermediate pixel values. This group of approaches replies on the weak smoothness assumption and therefore, the generated high-resolution images suffer from visual artifacts such as aliasing, jaggies, and blurring.

To generate results with sharper edges, reconstruction-based image SR tends to enforce certain statistical priors during the estimation of the target image. Within this group of SR methods, gradient profiles [23], [24] are popularly explored to describe the edge statistics due to its easily modeled heavy-tailed distribution [25]. Fattal [23] proposed a system that generates the gradient field of the high-resolution image based upon a statistical edge dependency relating edges of two different resolutions. In [24], Sun *et al.* performed a gradient field transformation to recover the high-resolution gradients provided the low-resolution image based on a parametric gradient profile model. A uniform parametric model for SR tasks is extremely challenging since it is difficult to capture the diverse characteristics of numerous natural images using a limited number of parameters.

Recently popularized example-based SR explores the relations between high-resolution and the corresponding low-resolution exemplars. Learning can be performed either via an external dataset [26]–[29], within the input image [30]–[33], or combined [34]. In later context we refer to them as external, internal, and hybrid example-based learning. External example-based learning methods aim to exploit the dependencies between high-resolution and low-resolution exemplars through a large image dataset. Coupled low-resolution/high-resolution dictionaries are popular representations for the raw patch exemplars or patch-related features. On the other hand, internal example-based SR is based upon the fact that small patches within a natural image tend to appear repeatedly within the image itself and across different resolutions. This redundancy is utilized in both image level [30]–[32] and the gradient level [33].

Zontak and Irani [35] have demonstrated the effectiveness of internal example-based SR under relatively small upscaling factors. However, the difficulty in estimating missing high-frequency details increases as the scaling factor gets larger due to the increment of low-resolution/high-resolution ambiguities. External example-based learning breaks the limitation by introducing new information from an external resource. However, by adopting a universal training dataset, performance of the external example-based SR depends on the similarity between the testing images and the training dataset. The lack of relevance between certain testing images or certain high-frequency patches in the testing images and a universal training dataset still exists. Keeping increasing the size of the training dataset provides a limited solution but still leaves the key problem untouched.

External example learning-based SR relies on learning priors or models from a large image dataset which leads to a stable SR performance. It is often less time consuming compared with internal-based approaches since the learning is normally performed off-line. On the other hand, internal patch redundancy has been validated to be powerful in recovering missing high frequency details [35]. To absorb the benefits in both external and internal example-based SR, a hybrid example-based single image SR framework was proposed in [34]. A proxy high-resolution image is first constructed through a set of pre-built regression models learned from external statistics. Afterwards, to recover the missing high-frequency details of the patches that are rarely seen in the training set, gradients of the proxy image are fed into a pyramid self-awareness framework guided by the input low-resolution gradients. Finally, the refined high-resolution gradients along with the input image are integrated into a uniform cost function to recover the final high-resolution image.

B. Sea Ice Motion Tracking

Sea ice motion through remote sensing data has been extensively studied since the appearance and wide availability of satellite imagery. As a side-note, although the term “motion” may strictly refer to continuous monitoring (e.g., through video), while imagery practically allows to detect displacements, or drifts, due to its common use in the literature, the term is used in this study interchangeably with the term “drift”. Sea ice drift is usually estimated with satellite imagery via a pattern matching method (e.g., [17], [36]). Sea ice drift vectors have been derived from a variety of satellite imagery utilizing a maximum cross-correlation (MCC) criterion [2], [13], [37].

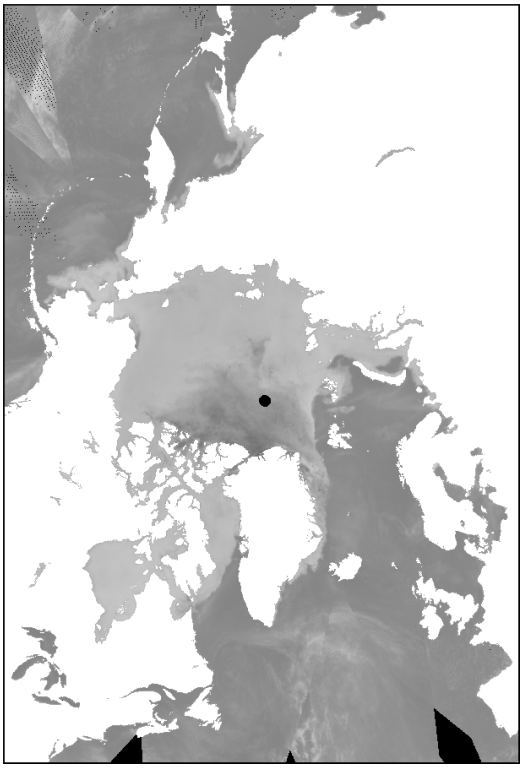

Fig. 1. Daily composite AMSR2 image at 36.5 GHz from January 1, 2013, projected on a polar stereographic grid. The latitude-longitude coordinates of the image corners are: upper-left $(30.98^{o}, 168.35^{o})$, upper-right $(31.37^{o}, 102.34^{o})$, lower-left $(33.92^{o}, 279.26^{o})$, lower-right $(34.35^{o}, 350.03^{o})$ [40].

These methods have been used successfully for sea ice motion for a variety of imagery, including visible [17], SAR [8], [38], scatterometer [39], and passive microwave [2].

A key factor in the pattern matching methods is that a characteristic and stable pattern, or a highly similar pattern, needs to be detected in both images of a pair to potentially retrieve a motion estimate. Visible and infrared sensors are limited by clouds, which are often prevalent in the Arctic regions. This substantially limits the number of motion vectors that can be retrieved. Likewise, other high-resolution sensors, such as SAR, have narrow swath widths and limited repeat coverage. Though having a much lower spatial resolution, passive microwave imagery has been especially useful for monitoring sea ice motion because it is independent of solar radiation, has complete daily coverage of the Arctic regions, and atmospheric interference is insignificant in most cases.

MCC-based approaches have been widely applied recently in sea ice drift estimation with several variations. Thomas *et al.* [41] proposed a method for sea ice motion characterization at a 400-m resolution vector field using European Remote Sensing Satellite-1 (ERS-1) SAR imagery. Motion fields of sea ice are obtained utilizing Phase Correlation (PC) pre-selection and MCC in a multi-resolution processing system. In [42], Thomas *et al.* developed a sea ice motion tracking system at the geospatial mesoscale (i.e., $1 - 100$ km^2) and proposed an adaptation of the algorithm that estimates drifts at close proximity to discontinuous regions using image inpainting. Building on this approach, Hollands and Dierking [43] implemented a PC- and MCC-based pattern matching algorithm to identify corresponding sea ice structure in a sequence of SAR images for the observation of high-resolution sea ice motions in the Weddell Sea at spatial resolutions varying from a few hundred meters to a few kilometers. Adapting the pattern matching approach in [41] by adding a Fourier-Mellin transform to capture rotational motion, Berg and Eriksson [44] recently proposed a hybrid pattern matching and feature tracking approach, the latter component requiring an image segmentation pre-processing step. Komarov and Barber [45] introduced an approach for automated selection of control points to which PC was applied to estimate candidate translational and rotational drifts, followed by MCC for the final decision. In [46], Lavergne *et al.* had earlier introduced a MCC-based sea ice motion tracking framework with a continuous optimization step for computing the motion vectors which are able to effectively reduce the quantization noise generated by MCC. This approach is proved capable of retrieving spatially smooth 48-h sea ice motion vector fields in the Arctic.

III. Data

In this paper, we employ AMSR2 data acquired from the JAXA Earth Observation Research Center[1]. Level 2 swath data of horizontal polarization 36.5 GHz brightness temperatures were gridded on a 12.5 km polar stereographic grid, tangent to the Earth's surface at 70 degrees northern latitude [40], using a simple drop-in-the-bucket method. All swaths from each day are averaged to create daily-average brightness temperature fields. The drift estimation algorithm is then applied to the gridded brightness temperatures. Seven daily such images from January 1-7, 2013 are employed, with the first one shown as an example in Fig. 1.

To further demonstrate the applicability of the proposed SR framework in tracking sea ice motion, a number of images derived from the Visible Infrared Imaging Radiometer Suite (VIIRS) on board the Suomi National Polar-orbiting Partnership (NPP) satellite[2] are used. The images are retrieved as a sequence of daily non-geolocated frames forming a video demonstrating the formation and motion of sea ice leads (cracks) around the Beaufort Sea along the northern coasts of Alaska and Canada. They include a total of 40 frames spanning from February 17 to March 18, 2013.

Finally, a set of $6,152$ natural images (non-satellite images) are used to train the regression models in the SR algorithm, as explained in Section IV-A. The training images are collected from the Berkeley segmentation dataset [47] and LabelMe dataset [48] which consist of a variety of natural images with different objects and scenes.

IV. Methods

To enhance the quality of the satellite imagery and to further increase the sea ice motion tracking accuracy, we propose a

[1]http://suzaku.eorc.jaxa.jp/GCOM_W/data/data_w_dpss.html

[2]http://www.nnvl.noaa.gov/MediaDetail2.php?MediaID=1310&MediaTypeID=3&ResourceID=104744

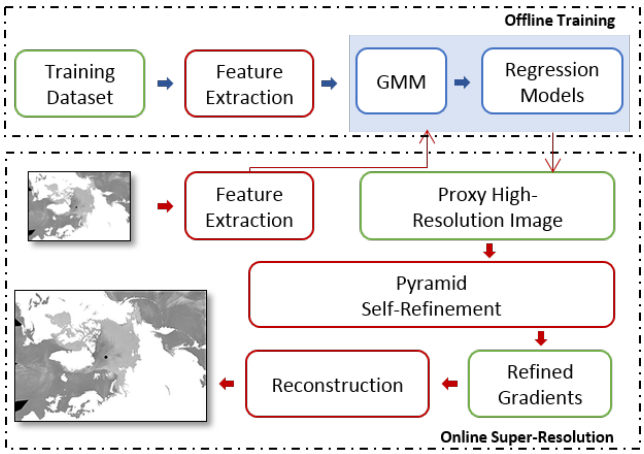

Fig. 2. Flowchart of the proposed hybrid example-based super-resolution algorithm. Provided a low-resolution image, a proxy high-resolution image is constructed through a set of regression models trained using an external image dataset. The input feature space is modeled with the Gaussian Mixture Models (GMM) to ensure a targeted and effective learning. With the proxy image, its gradients in both horizontal and vertical directions are refined utilizing corresponding gradients of the input image. The refined high-resolution gradients are then integrated into the reconstruction process to recover the final output high-resolution image.

sequential super-resolved sea ice motion tracking framework. The high-resolution satellite imagery is firstly constructed utilizing the hybrid example-based SR algorithm within which both external and internal statistics contribute to recover quality edges and fine details. Afterwards, a benchmark drift estimation algorithm is applied to show the superiority of performing motion tracking with the super-resolved finer scale imagery. In an additional experimental setting, a state-of-the-art object tracking algorithm is applied on super-resolved images to track individual sea ice objects (floes). The detailed steps are presented in the following subsections, respectively.

A. Super-Resolution

To improve the tracking accuracy of sea ice motion, a high-resolution image is firstly constructed out of the low-resolution input image using the hybrid exemplar-based SR approach [34]. Fig. 2 illustrates the schematic pipeline of the upsampling scheme. The system consists of three steps to upscale an input image: proxy image recovery from external statistics, gradient-level self-awareness from internal statistics, and final image reconstruction.

Provided an input low-resolution image, a proxy high-resolution image is generated with a set of pre-built regression models trained on a large natural image dataset. Due to the complicated characteristics revealed by the training images, the input feature space is modeled with the Gaussian Mixture Models (GMM) to ensure a targeted and effective learning. Afterwards, within each Gaussian component, an individual regression model is trained. Since the regression models are trained on a large external dataset with thousands of images, the constructed proxy high-resolution image generally has stable SR performance. However, due to the fact that a universal dataset is adopted for training, certain patches in the unseen input image may appear rarely within the training dataset and therefore lead to an over-smoothed prediction with missing high-frequency details. Thus, based on the fact that small patches tend to repeat themselves across scales, a gradient-level coarse-to-fine self-refinement is performed after obtaining the proxy image. Motivated by reconstruction-based SR approaches, a gradient-level refinement is adopted to better preserve the intensity changes. Finally, a fine quality high-resolution image is reconstructed through minimizing a cost function with the refined gradients.

In order to train the regression models, a large set of low-resolution/high-resolution exemplar patch pairs are firstly collected from an image dataset. All the images in the dataset are treated as high-resolution images and we generate the corresponding low-resolution images through a blur and down-sampling process as illustrated in Eq. (1):

$$L = (H * G)\downarrow_s, \tag{1}$$

where L and H stand for the low-resolution and high-resolution images, G represents the blur kernel, $\downarrow$ indicates the downsampling process and s is the scaling factor.

For a low-resolution/high-resolution patch pair $\{P_l, P_h\}$, we subtract the mean value of P_l from both patches to better preserve the structure information and eliminate the absolute value. After the subtraction and vectorization, the input low-resolution and high-resolution features are represented as $\boldsymbol{X} \in \mathbb{R}^{l\times M}$ and $\boldsymbol{Y} \in \mathbb{R}^{r\times M}$ respectively where l and r denote the corresponding feature dimensions and M indicates the number of training samples in total.

To ensure an effective learning of different edge and texture patterns, we first employ GMM to represent the feature distribution of the input low-resolution feature space. GMM is adopted due to the fact that it is a generative model with the capacity to model any given probability distribution function when the number of Gaussian components is large enough. GMM is based on a well-defined statistical model and is computationally tractable. In our experiment, $200,000$ randomly sampled features are utilized to estimate the GMM parameters of K components. We then assign each low-resolution feature $\boldsymbol{x}_i \in \boldsymbol{X}$ to corresponding Gaussian component with the highest probability.

Suppose there are M_k patches associated with the k-th Gaussian component and $\boldsymbol{X}_k \in \mathbb{R}^{l\times M_k}$, $\boldsymbol{Y}_k \in \mathbb{R}^{r\times M_k}$ represent the corresponding low-resolution/high-resolution features, a linear regression model is then trained with the regression coefficient A_k learnt through:

$$A_k^* = \underset{A_k}{\operatorname{argmin}}\{|\boldsymbol{Y}_k - A_k\hat{\boldsymbol{X}}_k|^2\}, \tag{2}$$

in which $\hat{\boldsymbol{X}}_k^T = [\boldsymbol{X}_k{}^T \ \mathbf{1}]$. During the testing phase, provided a low-resolution image, patch-based features are extracted by performing normalization and vectorization same as shown in the training phase. Then each feature is assigned to a Gaussian component according to the posterior where the corresponding regression model is applied to obtain the high-resolution patch. We employ simple averaging to blend overlapping pixels to generate the proxy high-resolution image.

To recover the missing high-frequency details for patches that are not frequently seen during training, a gradient-level self-awareness step is executed afterwards. As demonstrated experimentally in [34], patches with higher variances tend to appear less frequently within a natural image dataset. To refine the proxy high-resolution image H^p with the low-resolution input image L, patches in H^p (size $a \times a$) with variance larger than a pre-set threshold θ are extracted. Then for each high variance patch, its k most similar patches are searched and extracted within L where the similarity of two patches is measured in their mean square error. The next step is to combine the k found patches in a softmax way and replace the original patch with it.

The above self-awareness step is performed in the gradient level rather than directly in the image level because gradients better describe edges and textures due to the heavy-tailed distribution. Moreover, gradient patches are mostly flat with small variances. Therefore, only a small portion of the patches need to be adjusted which leads to an efficient refinement process. To be more specific, after obtaining the proxy image, its gradients in the horizontal and vertical directions are computed and refined with the corresponding gradients of the input image.

It is validated in [30] that average patch recurrence across scales decays as the resolution difference increases. Therefore, in the self-awareness step, if the scaling factor s is larger than 3, the refinement is executed in a coarse-to-fine manner. To ensure a more effective refinement, all the patches are normalized to have zero means and unit standard variances. The combined gradient patch is then adjusted based on the original mean and variance of the input patch.

The final high-resolution image is constructed from the self-refined high-resolution gradients and the input image by optimizing the following cost function:

$$H^* = \underset{H}{\operatorname{argmin}}\{|\nabla H - \nabla H_r|^2 + \alpha|(H * G)\downarrow_s - L|^2\}, \quad (3)$$

where ∇H_r represents the refined gradients after the pyramid gradient-level self-awareness step. G stands for a Gaussian kernel with standard variance σ that varies for different scaling factors s: $\sigma = \{0.8, 1.2, 1.6\}$ for $s = \{2, 3, 4\}$. α is the weighting factor. The cost function consists of constraints in both the gradient-level and the image-level. The first term presents constraint imposed by the refined high-resolution gradients. The second constraint ensures the consistency between the output and the input images. The cost function can be optimized through the gradient descent algorithm. Details of the parameters can be found in Section V-A.

B. Sea Ice Drift Estimation

The MCC method essentially matches patterns (e.g., grid cells) in two coincident images separated by a time interval through the use of a sliding window within a given neighborhood of the pattern's location in the first image. The new location of the pattern in the second image is determined by searching for the location of the sliding window where the cross-correlation with the pattern in the first image is maximized. The motion estimate can be calculated in a straightforward manner by dividing the displacement distance by the time separation between the two images. In this study, the MCC-based method proposed in [17] is applied for drift estimation. Besides the Advanced Very High Resolution Radiometer (AVHRR) data used in [17], this method has been used with AMSR-E data in [13] and operationally applied to passive microwave imagery as a component in a sea ice motion product distributed by the National Snow and Ice Data Center (NSIDC) [11].

The spatial resolution is a limiting factor in drift estimation accuracy since in theory the displacement can only be determined in discrete increments corresponding to the grid resolution. In the method employed, an oversampling procedure is conducted to calculate motion at subpixel resolutions by moving the sliding window in increments of $1/4$ of a grid cell instead of complete grid cells, in each direction [2], [9]. This is performed by implicitly applying linear interpolation that sets the value of the sub-grid cells equal to the weighted average of the original ones; e.g., for a $1/4$ sub-grid cell, it weighs the original grid cell 75% and the next grid cell 25%. With this oversampling procedure, sea ice drifts are expressed as displacements of products of the $1/4$ of the original grid resolution, so the motion vector field resolution, i.e., the minimum expressed displacement is $3,125$ m, or 3.62 cm s^{-1} for sequential day images. Thus, a drift larger than half of one sub-grid cell, i.e., $1/8$ of an image pixel or $1,562.5$ m, will be able to dominate the sub-grid cell value and be detected as drift by the algorithm—though, expressed as the minimum possible $3,125$ m drift. Besides oversampling, other subpixel motion estimation approaches have been applied in the literature as part of MCC-based motion estimation, such as curve fitting in the correlation value domain [8] or interpolation in the image data [46]. They could be used instead of oversampling in the MCC-based motion estimation on the images generated after applying the SR algorithm, i.e., still in tandem with the SR approach, and comparison of them could be a topic for future research. In this paper, staying consistent with the algorithm as applied in [17], [13], and [11], we use a $4\times$ oversampling as described above.

Post-processing quality control of the estimated motion vectors is then performed via two filtering approaches. First, a minimum correlation threshold is applied to remove marginal pattern matches that are more likely to be in error. Thresholds of 0.1 and 0.4 were selected in [17] for AVHRR data, 0.6 in [10] for scatterometer data, whereas 0.7 in [13] for 36.5 and 89 GHz AMSR-E data; in our case, a threshold of 0.6 is selected after experimentation. Second, a spatial coherence filter is used to remove outlying displacements by comparing each motion vector with neighboring vectors. If one vector is an outlier (i.e., the number of neighboring vectors whose displacements are within 2 pixels of this vector is less than two), it is deemed to be erroneous and should be removed. This is effective because generally large-scale motion is correlated at distances up to several hundred kilometers.

Motion errors are dependent on several factors, such as the geolocation accuracy of the input imagery, the validity of the assumption that the surface properties do not change between

images, atmospheric interference, and the spatial resolution of the imagery. Detecting motion during summer is challenging because of surface melt and more atmospheric emission by the moister atmosphere; thus, here we focus on winter scenes. As in [17], a land mask is employed to identify and exclude all land pixels from the motion vector computations.

While each of the above contributes to the total error, the most significant limitation in the accuracy of ice motions is the spatial resolution of the source imagery. With the AMSR2 36.5 GHz data mapped to a 12.5 km resolution grid, the motion can only be detected if it moves at least one half grid cell during the chosen time interval (one half sub-grid cell when oversampling is performed, as detailed above). Higher frequency imagery, at 89 GHz, can also be used and has roughly double the spatial resolution, gridded at 6.25 km. However, the 89 GHz is more susceptible to atmospheric interference and for AMSR-E, the 36.5 GHz channels yielded motion errors of a similar magnitude as the 89 GHz channels [13]. There is also uncertainty due to the use of daily average passive microwave images, where all swaths over 24 hours are averaged into a daily composite. This results in an ambiguous time interval because a 24-hour separation is assumed for all grid cells in the images. Thus, the retrieved pattern displacements are not associated with a distinct instant in time and results in a temporal smearing of the ice signal and distortion of surface patterns that inhibits correlation comparisons between days. However, daily composite microwave images have been preferred in several research studies [2], [13], [37] and operational products [11], since they reduce missing brightness temperature values and allow drifts to be calculated at the whole grid.

Fortunately, many errors are independent, including estimates from the same location at different times. This means that while individual vector estimates may have large errors, on average the errors are much smaller than the theoretical error and, importantly, the estimates are largely unbiased. For AMSR-E, the RMS error of daily motion speed has been found to be on the order of 6 cm s^{-1} with directional RMS values on the order of $15-20$ degrees [12], [13], [38].

A 6 cm s^{-1} is a reasonable uncertainty for looking at large scale sea ice circulation, particularly when tracking ice over several days and weeks. Under this circumstance, it is not possible to detect fine scale motions such as lead formation (openings in the ice) and ridging (convergent motion), which occur at scales of 1 km or less over subdaily intervals (corresponding to a speed of less than 1 cm s^{-1} over a day). These fine scale motions are important for local and regional processes (e.g., energy fluxes between the ocean and atmosphere) and for navigational guidance.

C. Sea Ice Object Tracking

In addition to the estimation of sea ice drifts, we further evaluate the potential of the images generated by the proposed SR approach to track specific sea ice moving objects (floes). Whereas the outcome of the MCC-based drift estimation method is a set of motion vectors representing the displacement or velocity of sea ice on the image grid, the outcome of the tracking method is a bounding box indicating the position of a specified object on each frame of a series of images.

Having as input the sequence of the Suomi NPP images, as described in Section III, we select a sea ice object in the first frame, i.e., the first image of the sequence, by manually defining the rectangular bounding box enclosing the object. Then, we apply the context tracker algorithm [18] to identify the position of the sea ice object on the next images of the sequence. The algorithm has proven effective in computer vision tracking applications in unconstrained environments. One main reason for its selection here is its performance in tracking an object in the presence of similar neighboring ones that might cause confusion, e.g., similarly looking sea ice objects, and small changes in appearance. It works by defining a set of so-called distracters and supporters. Distracters are regions with appearance similar to the tracking object that co-occur with it in several frames and might be potential sources of confusion. The algorithm tracks the distracters in addition to the selected object to prevent such confusion and false detection, even if the object is occluded in some frames. The supporters are extracted key points around the targeted object which move together with it and help the tracking. Both of them are automatically explored using a sequential randomized forest, an online template-based appearance model, and local features.

V. Results and Discussions

In this section, the proposed sequential super-resolved fine scale sea ice motion estimation system is evaluated with a sequence of passive microwave images. The dataset used for motion estimation is publicly available to allow reproduction or comparison of the results[3]. We also test the hybrid example-based SR method on tracking a selected sea ice object in a sequence of images from the Suomi NPP satellite. In both scenarios, there is an obvious boost in the tracking performance upon the super-resolved images.

A. Parameter Settings

The training dataset used for regression model learning is the same as in [34] which consists of $6,152$ natural images. We do not utilize satellite images for training due to the fact that natural images generally have much higher resolutions. All patches with size 7×7 from low-resolution images are extracted with corners of each patch removed. The central $3s\times 3s$ pixels in the corresponding high-resolution patch are utilized to formulate the high-resolution feature in which s is the magnification factor. The GMM model with 512 components is trained upon $200,000$ randomly selected low-resolution/high-resolution feature pairs. Afterwards, each feature is assigned to a Gaussian component with the highest probability. Then within each Gaussian component, a linear regression model is learnt with maximum $1,000$ low-resolution/high-resolution instances.

The maximum scaling factor is set to 3 in a single step in the pyramid gradient-level self-awareness. If the scaling factor s is

[3]http://media-lab.ccny.cuny.edu/wordpress/Code/sea_ice_flow_dataset.zip

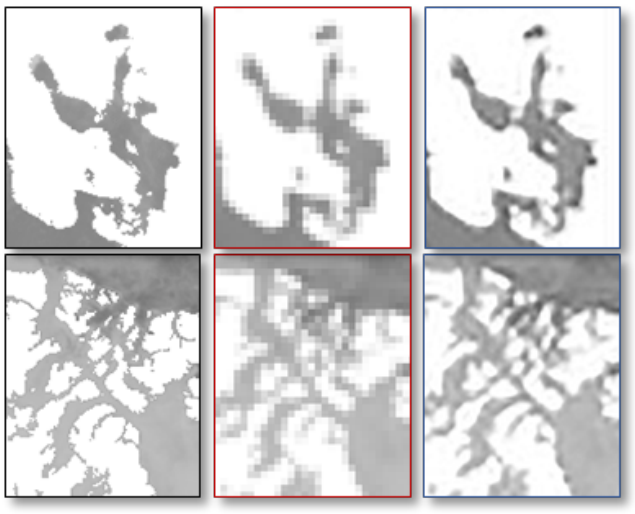

Fig. 3. Super-resolution of the passive microwave imagery (with scaling factor of 4). From left to right, the columns represent zoom-ins of the ground-truth image, the low-resolution image, and the generated high-resolution image. It is clearly indicated that the hybrid example-based super-resolution approach reconstructs the ice contours with minimal artifacts consistent with the ground-truth instances. This figure is better viewed on screen with high-resolution display.

larger than this threshold, a coarse-to-fine scheme is adopted with a factor of $\sqrt{s}$ per step. Patch size a in the self-refinement is 7 and the pre-set threshold θ is 5. During the search, the number k of the similar patches is set to be 5. Following experimentation, we assign α in Eq. (3) to $4/7$ to ensure both stable SR performance and fast convergence.

B. Drift Estimation

To demonstrate the effectiveness of the super-resolved fine scale sea ice motion tracking, the proposed framework is evaluated over the sequence of the AMSR2 passive microwave images from January 1-7, 2013. Provided the ground-truth (original AMSR2) imagery, we first generate low-resolution inputs of 50 km pixel spacing, by downsampling them under a scaling factor of 4. After that, the hybrid example-based SR algorithm is applied on the low-resolution images to generate the high-resolution instances with the same magnification factor 4. It is noteworthy that in a real application, the SR process would be applied on the original images, creating new images of 3.125 km spatial resolution. The reason of applying the SR process on the 50 km downsampled data and not the 12.5 km original ones, is the lack of images of spatial resolution higher than 12.5 km that we could use as ground-truth to evaluate the SR images against. Since only 12.5 km resolution images are available, we use these as ground-truth and create images of the same resolution, to demonstrate how accurately the SR process can increase the resolution of the input images (i.e., the 50 km ones) by 4 times and approximate the ideal high resolution images (i.e., the 12.5 km original AMSR2 images). For ease of interpretation and direct comparison with the super-resolved imagery, we upscale the 50 km input images to the same size as the ground-truth images using nearest-neighbor (NN) interpolation and use the interpolated results as the low-resolution inputs to perform motion estimation.

Fig. 3 presents the zoom-in comparisons before and after the hybrid example-based SR algorithm. Compared with the ground-truth instances, fine details and high quality edges are recovered with minimal visual artifacts after the SR.

Following the generation of the NN and SR images, the MCC-based drift estimation algorithm is applied on all pairs of consecutive days from each of the original AMSR2, NN, and SR image sets. Fig. 4 draws an example of the motion vector fields (velocities) resulting from the three image sets for the image pairs of January 1 and 2. The results cover the whole Arctic area and they are restricted to areas with sea ice. Areas of land and areas of sea and ocean not covered by ice are masked out. Zero-magnitude vectors are not drawn in the figure. It is readily seen that zero-magnitude vectors are much more common in the NN vector field than the SR field, i.e., the algorithm cannot detect sea ice drift in the NN image pair in the extent it does in the SR pair. It is also noted that the magnitude of the vectors estimated with the SR pair is closely related with the vectors from the original image pair. On the contrary, several vectors from the NN pair appear an order of magnitude larger than the original image pair vectors, even exceeding values of 70 cm s^{-1} [11] and 100 cm s^{-1} [49] considered as maximum realistic velocities. In particular, whereas the maximum velocities estimated for the original and SR pairs are 36.9 cm s^{-1} and 50.1 cm s^{-1}, respectively, the maximum one for the NN pair is 157.1 cm s^{-1}. The results are similar for the image pairs from the rest studied days.

Fig. 5 offers a close-up look of Fig. 4 for the main Arctic region around the North Pole. The motion vector field from each image set appears in a separate figure. In addition to the observations discussed above, Fig. 5 highlights the similarities in the distribution of the non-zero-magnitude vectors between the original (Fig. 5a) and the super-resolved (Fig. 5c) images. In a large area around the North Pole (black dot near the center of the images), the SR images are able to reveal drifts in a much closer detail than the NN images, which are incapable of depicting small sea ice displacements. On the contrary, the NN images result in the erroneous detection of large-extent drifts in a region where the two other image sets detect small or no drifts (western part of the region, Fig. 5b). This suggests the existence of intense image artifacts in the NN images, in contrast with the smoother results by the SR images. As a note, since all land pixels are excluded from the motion vectors calculations in all images, any artifacts in the NN and SR images in the land pixels, and to a large degree in the coastlines, are expected to have only small effect in the estimated motion vectors.

To quantitatively evaluate the benefits from the super-resolved images compared with the low-resolution NN ones, Fig. 6 draws the scatterplots of the x-axis (vertical) and y-axis (horizontal) drifts from the two image sets, compared with the respective drifts from the original AMSR2 images considered as ground truth, for the image pairs on January 1 and 2. Several outliers can be noticed for the NN drift vectors in both axes (Fig. 6a and 6b), whereas the distribution of data in the SR is more compact. In addition, the least squares linear regression

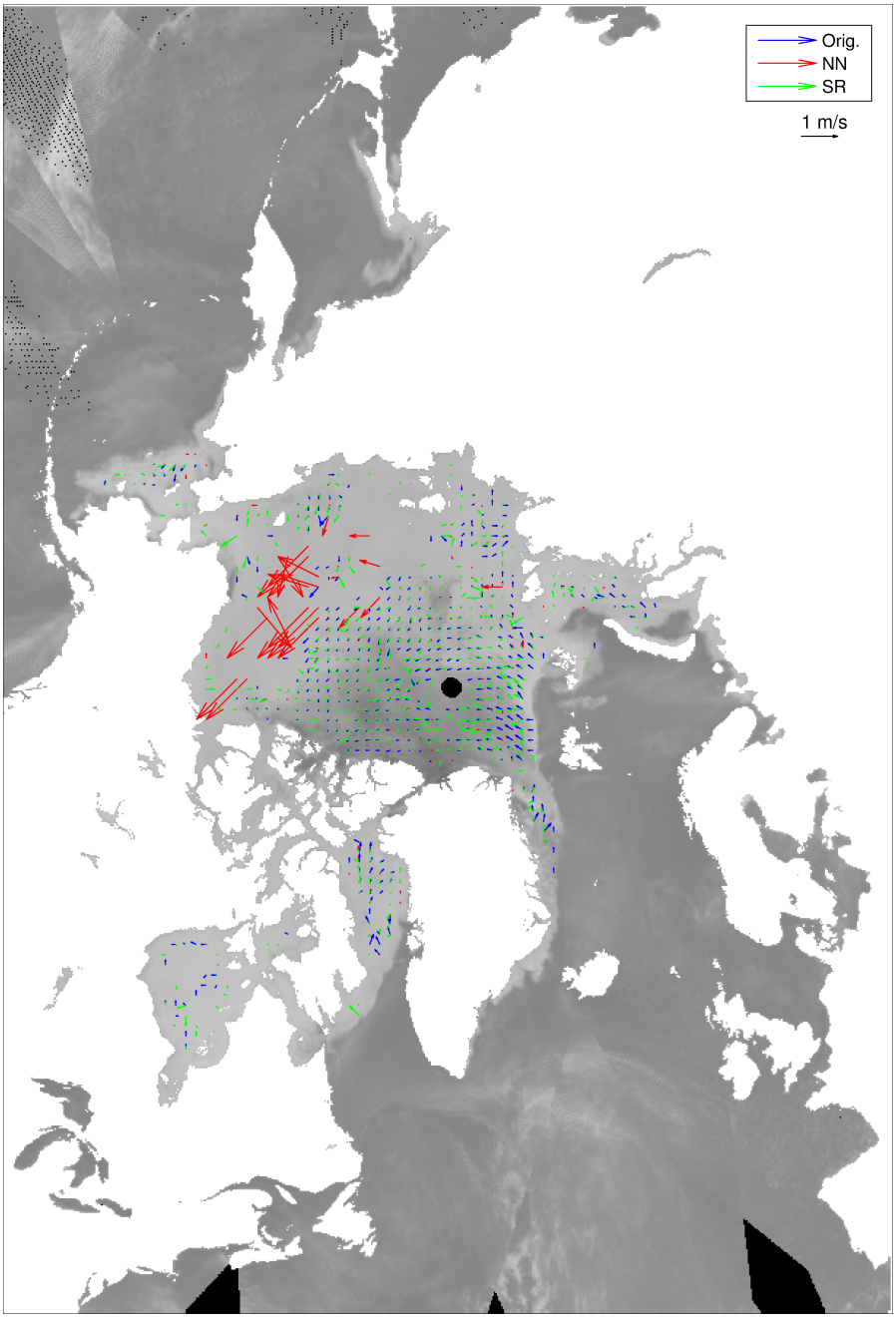

Fig. 4. Estimated motion vectors from the first pair (January 1-2, 2013) of images, for each of the original AMSR2 (Orig.), low-resolution nearest-neighbor (NN), and super-resolution (SR) image sets.

fit line is calculated for each image pair and axis drift and drawn as a solid line; the 1-by-1 ideal correlation between the NN or SR results and the original data is drawn as a dashed line. As observed, the fitting lines for the drifts in the SR images (Fig. 6c and 6d) are closer to the ideal-fit line than the one in the NN images (Fig. 6a and 6b), revealing that the correlation between SR and original image vectors is higher compared with the correlation between the NN and original image vectors.

Table I provides a thorough quantitative evaluation of the NN and SR motion vectors compared with the original image data considered as ground-truth. As observed, the relative squared error ("RSE"), root mean squared error ("RMSE"), and mean absolute error ("MAE") are consistently smaller for the SR vectors than the NN ones for both the vertical and horizontal drifts and all image pairs. On the contrary, the Pearson correlation coefficient ("P") is significantly higher for SR vectors compared with the NN vectors. This shows that there is a strong positive correlation between the SR and original vectors in several cases, whereas on the contrary, almost no, or even slightly inverse (for Jan 2-3 pair and y-axis), correlation appears for NN vectors.

Fig. 7 plots the error distributions (in km) of the NN and SR motion vectors in the two axes, compared with the vectors

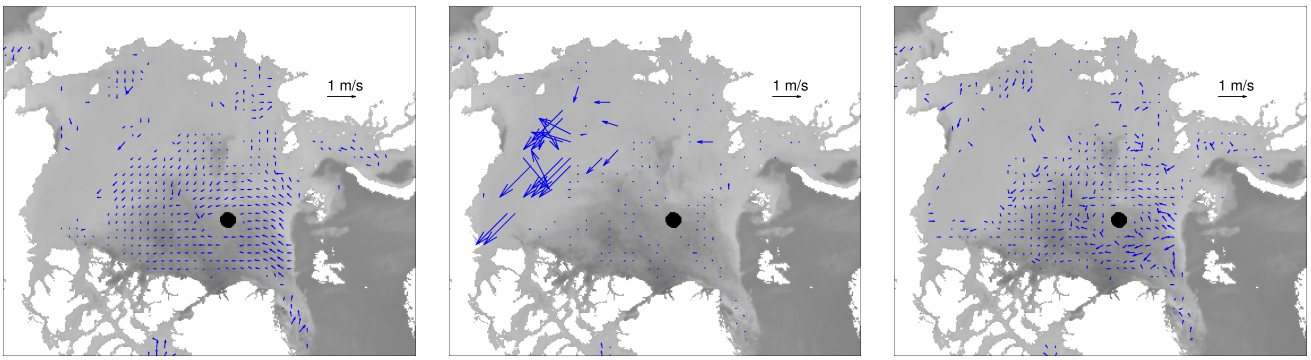

(a) (b) (c)

Fig. 5. Close-up look for the main Arctic region around the North Pole of the estimated motion vectors from the first pair (January 1-2, 2013) of images, for the (a) original AMSR2 (Orig.), (b) low-resolution nearest-neighbor (NN), and (c) super-resolution (SR) image sets.

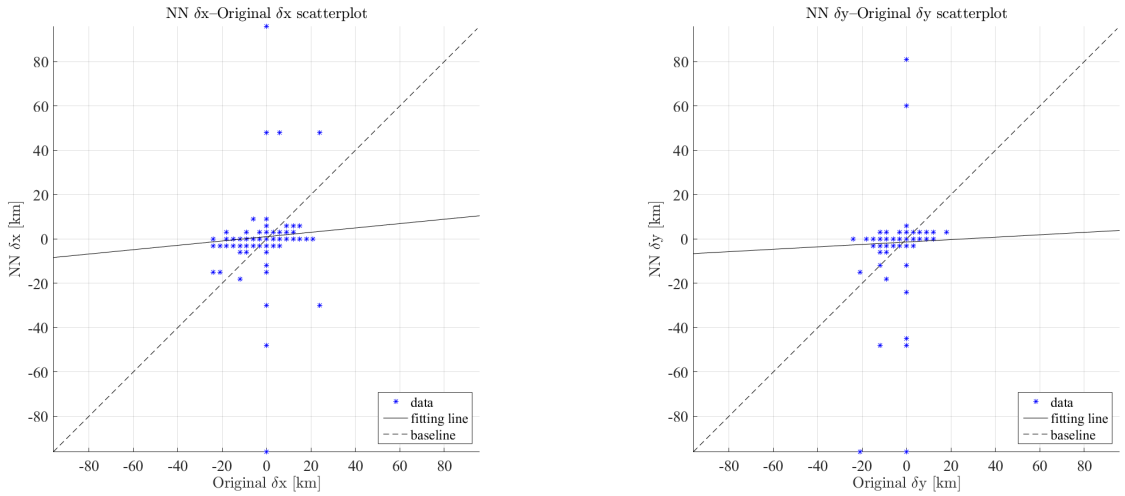

(a) (b)

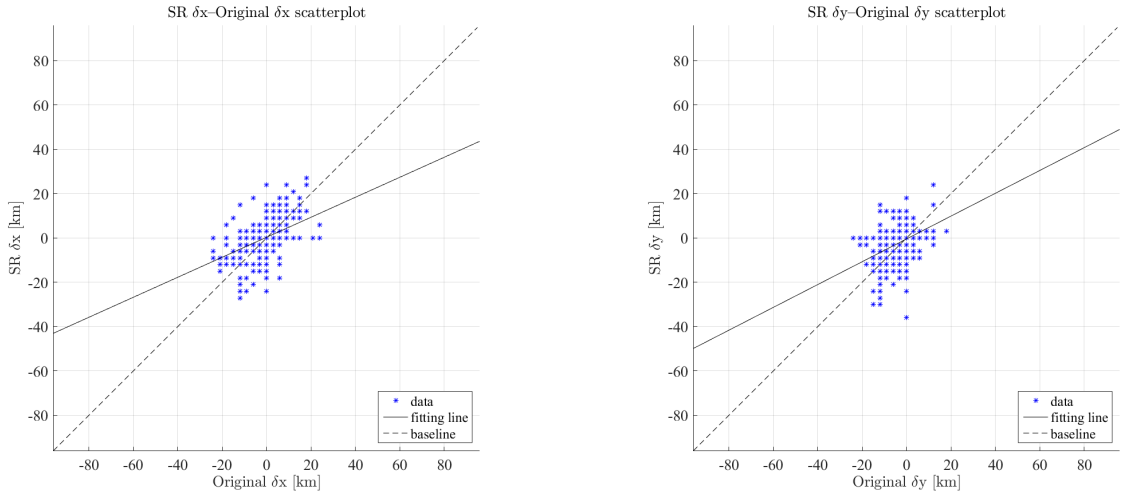

(c) (d)

Fig. 6. Scatterplots of NN and SR drift estimates (in km) in the two axes compared with the vectors from the original images considered as ground-truth, for the image pairs on January 1 and 2. (a) NN drift in the x-axis (vertical); (b) NN drift in the y-axis (horizontal); (c) SR drift in the x-axis; (d) SR drift in the y-axis. In addition to the drift data, the 1-by-1 ideal match line is drawn as dashed line, as well as the least squares linear regression fit line as solid one.

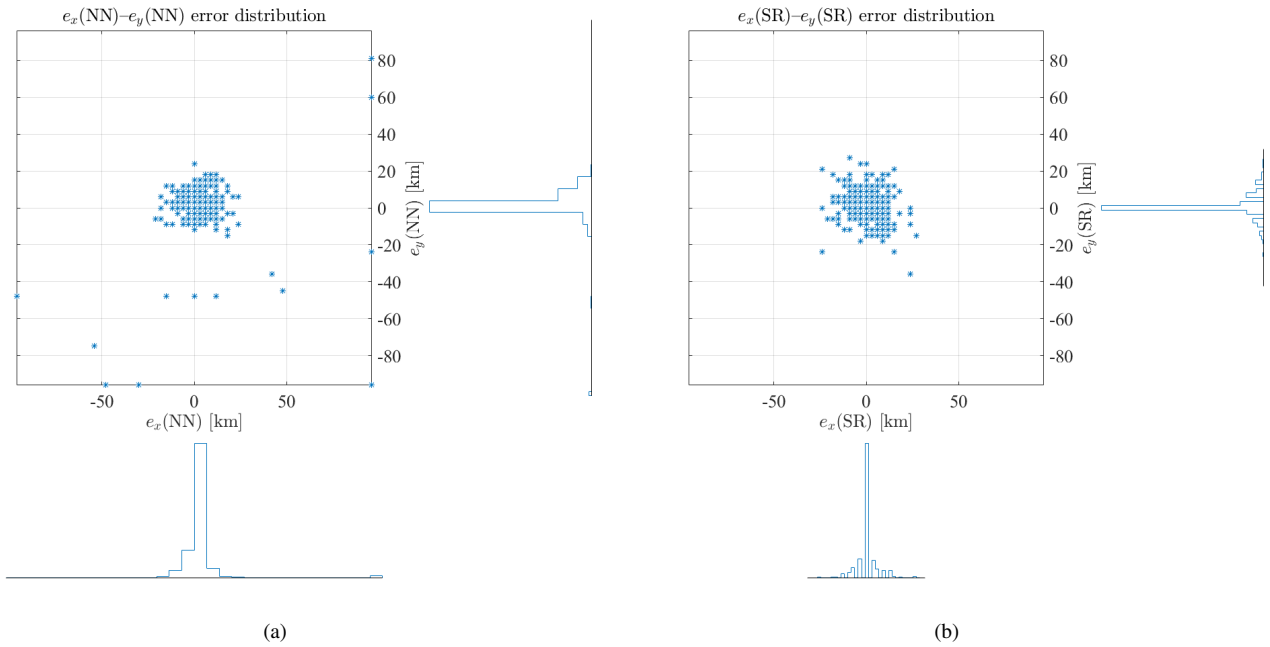

(a) (b)

Fig. 7. Error distributions from the (a) NN and (b) SR drift estimates in the two axes compared with the vectors from the original images considered as ground-truth, for the image pairs on January 1 and 2. The histograms of the probability distribution functions appear on the bottom and right part of the plot, for the x- and y-axis drifts, respectively.

from the original images, for the image pair Jan 1-2. Apart from a slight bias on the positive direction in the x axis, no significant biases are observed in the two vectors sets. However, a number of extreme error values (outliers) can be observed in both axes of the NN vectors. This seems to partially affect the standard deviation of the distribution which appears larger than the SR respective one for both axes in the schematic representation of the probability density function histograms appearing below and on the right of the main plot areas. In fact, the standard deviations of the errors for the SR vectors are consistently lower for all image pairs than the NN vectors, as seen in Table II. This reveals the lack of outlier vectors in the SR images and the close relevance with the vectors from the original data. The mean values of the errors are closer to zero for the SR vectors than the NN vectors, showing a smaller bias towards negative or positive drifts. Regarding differences between the x and y directions, no strong biases in one versus the other direction are observed in either the NN or the SR data.

C. Object Tracking

Similar as the previous experiments, we apply context tracker [18] to the low-resolution input frames and the super-resolved frames for comparison. By comparing the tracking results with the ground-truth results, a boost in the tracking performance is observed after SR.

Fig. 8 illustrates the tracking comparisons over the selected frames of the whole sea ice movement period. Three different ice fragments are tracked as marked in bounding boxes with different colors. The bounding boxes are manually labeled and are the same in the starting frame. As observed, starting from frame 12 (i.e., on Feb. 28), context tracker is unable to locate one of the ice fragment instance (marked in red) within the low-resolution input. However, on the contrary, the tracking results over the corresponding super-resolved frame are almost identical compared with the ground-truth. As time goes by, context tracker failures keep occurring in the low-resolution inputs for other ice fragment instances. On the other hand, the tracking performance over the super-resolved imagery is stable and accurate.

The success plots for the NN and SR images are calculated to quantitatively evaluate their tracking performance compared with the tracking results from the original images, as a widely employed evaluation measure in object tracking [50]. For each image and object, the overlap score, or *intersection-to-union ratio*, between the region of the object bounding box, r_t, and the respective ground-truth bounding box from the original image, r_o, is calculated as $d = |r_t \cap r_o|/|r_t \cup r_o|$, where the nominator and denominator represent the intersection and union between the two regions, respectively. The tracking is considered correct if d is larger than a pre-defined threshold, d_0. For each of the three objects, the ratio of the number of frames (images) where the object is correctly detected to the overall number of frames is calculated. The average ratio over the three objects is the success rate, S, for the specific type of image and overlap threshold. To make the evaluation more robust, we calculate S for different values of d_0 ranging from 0 to 1 (with a step of 0.05). The Area Under Curve (AUC) is also calculated for the NN and SR plots, as a further quantitative measure of their agreement with the ground truth results. The generated plots are provided in Fig. 9. As expected, S generally decreases as d increases, since the requirement for a

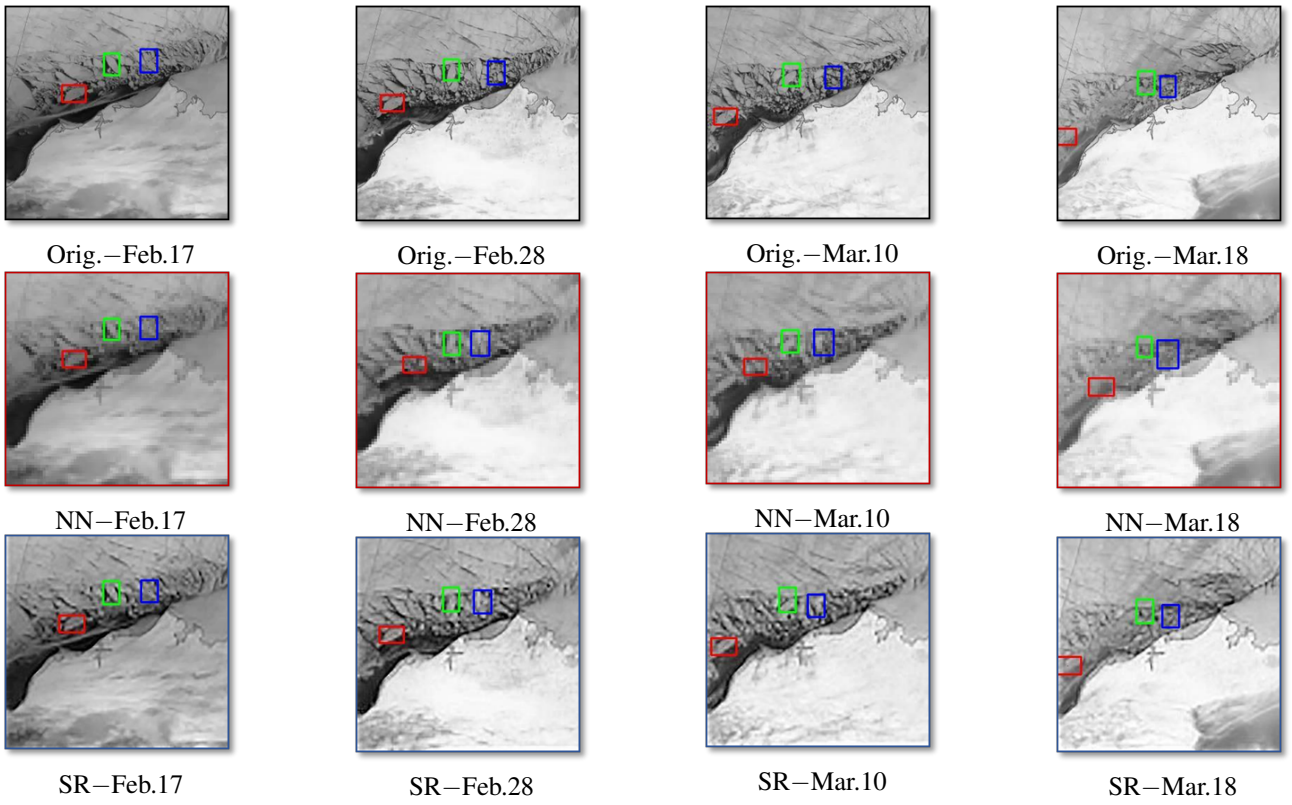

Fig. 8. Tracking comparisons of sea ice fragments around the Beaufort Sea spanning from Feb. 17 to Mar. 18 in year 2013. The rows represent the tracking results on the ground-truth images (Orig.), the low-resolution input images (NN), and the generated high-resolution images (SR), respectively, for 4 indicative dates. Three ice fragment instances are tracked in the sequential frames as marked in bounding boxes with different colors. Context tracker [18] loses track of the tracking instances in low-resolution instances but keeps a stable performance over the super-resolved frames. This figure is better viewed on screen with high-resolution display.

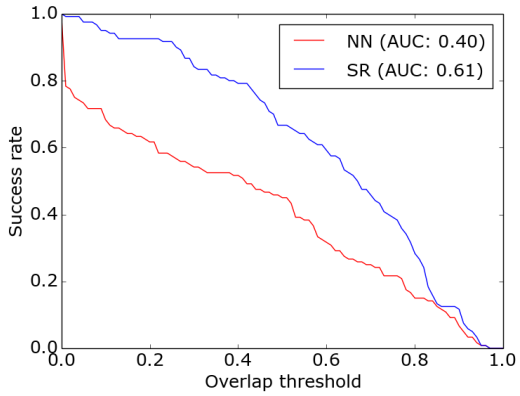

Fig. 9. Success plots of the three-object tracking with the NN and SR Suomi NPP images compared with the results from the original images, for different overlap thresholds. The Area Under Curve (AUC) values are also provided.

correct matching gets stricter. As readily seen, the success rate for the SR images is significantly higher than the NN images, for almost the entire range of overlap thresholds. In particular, S for the NN images drops by around 20% immediately after $d_0 > 0$ is applied. On the contrary, S remains above 0.8 for the SR images until $d_0 = 0.4$. The AUC value for NN is 0.40, whereas for SR it is 0.61, more than 50% higher.

TABLE I
QUANTITATIVE EVALUATION OF THE LOW-RESOLUTION NEAREST-NEIGHBOR (NN) AND SUPER-RESOLUTION (SR) DRIFT VECTORS COMPARED WITH THE VECTORS FROM THE ORIGINAL AMSR2 IMAGES, FOR ALL IMAGE PAIRS INDIVIDUALLY AND AGGREGATED. "δX" AND "δY" INDICATE THE DRIFTS ON THE VERTICAL AND HORIZONTAL AXES, RESPECTIVELY. "SAMPLES" STAND FOR THE TOTAL NUMBER OF DRIFT VECTORS COMPARED, "RSE" FOR THE RELATIVE SQUARED ERROR, "RMSE" THE ROOT MEAN SQUARED ERROR IN KM, "MAE" THE MEAN ABSOLUTE ERROR IN KM, AND "P" THE PEARSON CORRELATION COEFFICIENT.

		δx				δy			
Dates	Samples	RSE	RMSE	MAE	P	RSE	RMSE	MAE	P
NN									
Jan 1–2	1165	6.16	12.22	3.82	0.04	6.94	12.28	4.08	0.02
Jan 2–3	1163	5.03	13.14	4.66	0.09	3.34	12.73	4.79	-0.01
Jan 3–4	1120	3.34	11.26	4.10	0.12	2.80	12.54	4.87	0.04
Jan 4–5	1121	4.56	12.11	3.56	0.01	2.40	12.75	5.80	0.07
Jan 5–6	1118	1.96	6.81	2.31	0.06	1.22	10.43	5.88	0.37
Jan 6–7	1117	5.00	10.15	3.10	0.04	2.13	12.83	5.87	0.34
Total	6804	4.29	11.16	3.60	0.06	2.51	12.29	5.21	0.16
SR									
Jan 1–2	1165	1.15	5.28	2.75	0.44	1.26	5.22	2.70	0.46
Jan 2–3	1163	1.00	5.85	3.04	0.55	0.86	6.45	3.06	0.52
Jan 3–4	1120	0.80	5.50	2.59	0.58	0.72	6.36	2.97	0.59
Jan 4–5	1121	1.17	6.13	2.67	0.36	0.70	6.86	3.43	0.62
Jan 5–6	1118	1.82	6.57	3.04	0.20	0.72	8.01	3.81	0.63
Jan 6–7	1117	1.65	5.83	2.84	0.39	0.69	7.31	3.54	0.69
Total	6804	1.19	5.87	2.82	0.43	0.76	6.75	3.24	0.61

TABLE II
QUANTITATIVE EVALUATION OF THE ERRORS OF THE LOW-RESOLUTION NEAREST-NEIGHBOR (NN) AND SUPER-RESOLUTION (SR) DRIFT VECTORS COMPARED WITH THE VECTORS FROM THE ORIGINAL AMSR2 IMAGES, FOR ALL IMAGE PAIRS INDIVIDUALLY AND AGGREGATED. "μ_X" AND "μ_Y" STAND FOR THE MEAN ERROR VALUES IN THE X AND Y DIRECTIONS, RESPECTIVELY, WHEREAS "σ_X" AND "σ_Y" FOR THE RESPECTIVE STANDARD DEVIATION.

	NN				SR			
Dates	μ_x	μ_y	σ_x	σ_y	μ_x	μ_y	σ_x	σ_y
Jan 1–2	1.03	0.58	12.19	12.27	0.30	0.57	5.28	5.19
Jan 2–3	0.53	1.59	13.13	12.64	-0.67	1.02	5.82	6.37
Jan 3–4	1.05	1.36	11.21	12.48	0.23	0.60	5.50	6.33
Jan 4–5	1.05	1.31	12.07	12.69	0.23	0.11	6.13	6.86
Jan 5–6	0.00	2.09	6.81	10.22	-0.12	0.68	6.57	7.99
Jan 6–7	0.64	0.89	10.13	12.81	0.09	0.24	5.83	7.31
Total	0.72	1.30	11.14	12.23	0.01	0.54	5.87	6.73

VI. CONCLUSION

In this paper, we propose a novel sequential fine scale sea ice motion tracking framework in which the tracking performance is significantly improved using the super-resolved imagery. Provided an input low-resolution satellite imagery, the hybrid example-based super-resolution algorithm is employed to generate the corresponding high-resolution instance. Afterwards, a benchmark tracking method is applied to detect the sea ice motion.

As demonstrated by the experimental results, the proposed approach is effective in approximating the outcomes achieved by the native high-resolution data, and significantly outperforms the low-resolution data used for the generation of the super-resolved ones. We further demonstrate the transferability of the proposed framework in a different setting by applying a state-of-the-art object tracking algorithm in the super-resolved imagery. An obvious boost in the tracking performance is observed.

ACKNOWLEDGMENT

AMSR2 data was supplied by the GCOM-W1 Data Providing service, Japan Aerospace Exploration Agency (JAXA). We also thank Xuejian Rong for his valuable assistance during the preparation of the object tracking experiments.

REFERENCES

[1] CEOS Disaster Management Support Group, "Ice hazards," 2001. [Online]. Available: http://cryos.ssec.wisc.edu/docs/CEOS_ICE_HAZARDS_Report_2001.pdf, Accessed on: Jun. 22, 2016.

[2] W. N. Meier, J. A. Maslanik, and C. W. Fowler, "Error analysis and assimilation of remotely sensed ice motion within an Arctic sea ice model," *J. Geophys. Res.*, vol. 105, pp. 3339–3356, 2000.

[3] N. Kimura, A. Nishimura, Y. Tanaka, and H. Yamaguchi, "Influence of winter sea-ice motion on summer ice cover in the Arctic," *Polar Res.*, vol. 32, 2013.

[4] L. W. A. De Silva, H. Yamaguchi, and J. Ono, "Ice–ocean coupled computations for sea-ice prediction to support ice navigation in Arctic sea routes," *Polar Res.*, vol. 34, 2015.

[5] US National Ice Center, "The United States National Ice Center (NIC)," [Online]. Available: http://www.natice.noaa.gov, Accessed on: Jun. 22, 2016.

[6] C. Bertoia, M. Manore, and H. Andersen, "Mapping ice covered waters from space," *Backscatter*, vol. 12, no. 3, pp. 14–22, 2001.

[7] K. Partington, T. Flynn, D. Lamb, C. Bertoia, and K. Dedrick, "Late twentieth century Northern Hemisphere sea-ice record from U.S. National Ice Center ice charts," *J. Geophys. Res.*, vol. 108, no. 11, 2001.

[8] R. Kwok, A. Schweiger, D. Rothrock, S. Pang, and C. Kottmeier, "Sea ice motion from satellite passive microwave imagery assessed with ERS SAR and buoy motions," *J. Geophys. Res.*, vol. 103, no. 4, pp. 8191–8214, 1998.

[9] W. N. Meier and J. A. Maslanik, "Effect of environmental conditions on observed, modeled, and assimilated sea ice motion errors," *J. Geophys. Res.*, vol. 108, 2003.

[10] F. Girard-Ardhuin and R. Ezraty, "Enhanced arctic sea ice drift estimation merging radiometer and scatterometer data," *IEEE Trans. Geosci. Remote Sens.*, vol. 50, no. 7, pp. 2639–2648, 2012.

[11] M. Tschudi, C. Fowler, J. Maslanik, J. S. Stewart, and W. Meier, "Polar Pathfinder daily 25 km EASE-Grid sea ice motion vectors, version 3," Boulder, Colorado USA: NASA National Snow and Ice Data Center Distributed Active Archive Center, 2016. doi: http://dx.doi.org/10.5067/O57VAIT2AYYY.

[12] R. Kwok, "Summer sea ice motion from the 18 GHz channel of AMSR-E and the exchange of sea ice between the Pacific and Atlantic sectors," *Geophys. Res. Lett.*, vol. 35, 2008.

[13] W. N. Meier and M. Dai, "High-resolution sea-ice motions from AMSR-E imagery," *Ann. Glaciol.*, vol. 44, pp. 352–356, 2006.

[14] M. T. Merino and J. Nunez, "Super-resolution of remotely sensed images with variable-pixel linear reconstruction," *IEEE Trans. Geosci. Remote Sens.*, vol. 45, no. 5, pp. 1446–1457, 2007.

[15] F. Li, X. Jia, D. Fraser, and A. Lambert, "Super resolution for remote sensing images based on a universal Hidden Markov Tree model," *IEEE Trans. Geosci. Remote Sens.*, vol. 48, no. 3, pp. 1270–1278, 2010.

[16] S. Guo, S. Liu, S. Yang, and L. Jiao, "Remote sensing image super-resolution reconstruction based on nonlocal pairwise dictionaries and double regularization," *IEEE J. Sel. Topics Appl. Earth Observ. in Remote Sens.*, vol. 7, no. 12, pp. 4784–4792, 2014.

[17] W. Emery, C. Fowler, J. Hawkins, and R. Preller, "Fram Strait satellite image-derived ice motions," *J. Geophys. Res.*, vol. 96, no. C3, pp. 4751–4768, 1991.

[18] T. B. Dinh, N. Vo, and G. Medioni, "Context Tracker: Exploring supporters and distracters in unconstrained environments," in *CVPR*, 2011.

[19] J. Boulanger, C. Kervrann, and P. Bouthemy, "Space-time adaptation for patch-based image sequence restoration," *IEEE Trans. Pattern Anal. Mach. Intell.*, vol. 24, pp. 1096–1102, 2007.

[20] S. Farsiu, M. Robinson, M. Elad, and P. Milanfar, "Fast and robust multiframe super resolution," *IEEE Trans. Image Process.*, vol. 13, pp. 1327–1344, 2004.

[21] M. Protter, M. Elad, H. Tekeda, and P. Milanfar, "Generalizing the non-local-means to super-resolution reconstruction," *IEEE Trans. Image Process.*, vol. 18, pp. 36–51, 2009.

[22] B. Shi, H. Ben-Ezra, S. Yeung, C. Fernandez-Cull, R. Shepard, C. Barsi, and R. Raskar, "Sub-pixel layout for super-resolution with images in the octic group," in *ECCV*, 2014.

[23] R. Fattal, "Image upsampling via imposed edge statistics," in *ACM SIGGRAPH*, 2007.

[24] J. Sun, J. Sun, Z. Xu, and H. Shum, "Image super-resolution using gradient profile prior," in *CVPR*, 2008.

[25] J. Huang and D. Mumford, "Statistics of natural images and models," in *CVPR*, 1999.

[26] J. Yang, J. Wright, T. Huang, and Y. Ma, "Image super-resolution via sparse representation," *IEEE Trans. Image Process.*, vol. 19, pp. 2861–2873, 2010.

[27] J. Sun, J. Zhu, and M. Tappen, "Context-constrained hallucination for image super-resolution," in *CVPR*, 2010.

[28] R. Timofte, V. Smet, and L. Gool, "Anchored neighborhood regression for fast example-based super-resolution," in *ICCV*, 2013.

[29] C. Yang and M. Yang, "Fast direct super-resolution by simple functions," in *ICCV*, 2013.

[30] D. Glasner, S. Bagon, and M. Irani, "Super-resolution from a single image," in *ICCV*, 2009.

[31] G. Freedman and R. Fattal, "Image and video upscaling from local self-examples," *ACM T. Graphic.*, vol. 28, pp. 1–10, 2010.

[32] J. Huang, A. Singh, and N. Ahuja, "Single image super-resolution from transformed self-exemplars," in *CVPR*, 2015.

[33] Y. Xian and Y. Tian, "Single image super-resolution via internal gradient similarity," *J. Vis. Commun. Image R.*, vol. 35, pp. 91–102, 2016.

[34] Y. Xian, X. Yang, and Y. Tian, "Hybrid example-based single image super-resolution," in *ISVC*, 2015.
[35] M. Zontak and M. Irani, "Internal statistics of a single natural image," in *CVPR*, 2011.
[36] A. K. Liu, Y. Zhao, and S. Y. Wu, "Arctic sea ice drift from wavelet analysis of NSCAT and special sensor microwave imager data," *J. Geophys. Res.*, vol. 104, pp. 11 529–11 538, 1999.
[37] W. J. Emery, C. Fowler, and J. A. Maslanik, "Satellite-derived maps of Arctic and Antarctic sea-ice motion: 1988 to 1994," *Geophys. Res. Lett.*, vol. 24, no. 8, pp. 897–900, 1997.
[38] H. Sumata, R. Kwok, R. Gerdes, F. Kauker, and M. Karcher, "Uncertainty of Arctic summer ice drift assessed by high-resolution SAR data," *J. Geophys. Res. Oceans*, vol. 120, pp. 5285–5301, 2015.
[39] J. Haarpaintner and G. Spreen, "Use of enhanced-resolution QuikSCAT/SeaWinds data for operational ice services and climate research: Sea ice edge, type, concentration, and drift," *IEEE Trans. Geosci. Remote Sens.*, vol. 45, no. 10, 2007.
[40] National Snow and Ice Data Center, "Documentation: Polar stereographic projection and grid," [Online]. Available: http://nsidc.org/data/polar-stereo/ps_grids.html, Accessed on: Jun. 27, 2016.
[41] M. Thomas, C. Geiger, and C. Kambhamettu, "High resolution (400 m) motion characterization of sea ice using ERS-1 SAR imagery," *Cold Reg. Sci. Technol.*, vol. 52, pp. 207–223, 2008.
[42] M. Thomas, C. Kambhamettu, and C. Geiger, "Motion tracking of discontinuous sea ice," *IEEE Trans. Geosci. Remote Sens.*, vol. 49, no. 12, 2011.
[43] T. Hollands and W. Dierking, "Performance of a multiscale correlation algorithm for the estimation of sea-ice drift from SAR images: Initial results," *Ann. Glaciol.*, vol. 52, no. 57, pp. 311–317, 2011.
[44] A. Berg and L. E. B. Eriksson, "Investigation of a hybrid algorithm for sea ice drift measurements using Synthetic Aperture Radar images," *IEEE Trans. Geosci. Remote Sens.*, vol. 52, no. 8, pp. 5023–5033, 2014.
[45] A. Komarov and D. Barber, "Sea ice motion tracking from sequential dual-polarization RADARSAT-2 images," *IEEE Trans. Geosci. Remote Sens.*, vol. 52, no. 1, 2014.
[46] T. Lavergne, S. Eastwood, Z. Teffah, H. Schyberg, and L. Breivik, "Sea ice motion from low-resolution satellite sensors: An alternative method and its validation in the Arctic," *J. Geophys. Res.*, vol. 115, 2010.
[47] D. Martin, C. Fowlkes, D. Tal, and J. Malik, "A Database of Human Segmented Natural Images and its Application to Evaluating Segmentation Algorithms and Measuring Ecological Statistics," in *ICCV*, 2001.
[48] B. C. Russell, A. Torralba, K. P. Murphy, and W. T. Freeman, "LabelMe: A database and web-based tool for image annotation," *Int. J. Comput. Vision*, vol. 77, pp. 157–173, 2008.
[49] M. Leppäranta, *The Drift of Sea Ice*, 2nd ed. Berlin-Heidelberg, Germany: Springer, 2011.
[50] Y. Wu, J. Lim, and M.-H. Yang, "Online object tracking: A benchmark," in *IEEE Conf. Computer Vision and Pattern Recognition*, Portland, OR, 2013, pp. 2411–2418.

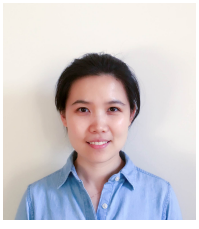

Yang Xian (S'14) received the B.E. degree from Southeast University, Nanjing, China, in 2009 and the M.S. degree from New York University, New York, USA, in 2012. She is currently pursuing the Ph.D degree in Computer Science at the Graduate Center, the City University of New York, New York, USA. Her research interests are in the synergic areas of computer vision, computational photography, and machine learning. She has been working on large-scale surveillance event detection, image captioning, and designing quality enhancement algorithms, i.e., super-resolution, completion, for both RGB images and depth maps.

Zisis I. Petrou (S'05–M'15) received the Diploma in electrical and computer engineering from the Aristotle University of Thessaloniki, Greece, in 2007 and the M.Sc. degree in space studies from the International Space University, Strasbourg, France, in 2009. In 2015, he received the Ph.D. degree in remote sensing from the Department of Electrical and Electronic Engineering, Imperial College London, United Kingdom.

In 2009, he was an Intern with the German Aerospace Center (DLR), Oberpfaffenhofen, Germany. From 2009 to 2016, he was a Research Assistant with the Centre for Research and Technology Hellas, Thessaloniki, Greece. Since February 2016, he has been a Postdoctoral Research Scholar with the City College of New York, City University of New York. His research interests include classification, motion detection and prediction analysis on remote sensing images using advanced machine learning, image processing, and computer vision techniques.

Dr. Petrou is a member of the Technical Chamber in Greece. He was the recipient of the Best Paper Award for Young Professionals under 35 at the 2nd International Conference on Space Technology, Athens, in 2011, sponsored by IEEE. He has been a scholar of the European Space Agency (ESA) and the Onassis Foundation, Greece.

YingLi Tian (M'99–SM'01) received the B.S. and M.S. degrees from Tianjin University, China, in 1987 and 1990, and the Ph.D. degree from Chinese University of Hong Kong, Hong Kong, in 1996.

After holding a faculty position at National Laboratory of Pattern Recognition, Chinese Academy of Sciences, Beijing, she joined Carnegie Mellon University in 1998, where she was a postdoctoral fellow at the Robotics Institute. She then worked as a research staff member in IBM T. J. Watson Research Center from 2001 to 2008. She is one of the inventors of the IBM Smart Surveillance Solutions. She is currently a professor in the Department of Electrical Engineering at City College and Graduate Center, City University of New York. Her current research focuses on a wide range of computer vision problems from motion detection and analysis, assistive technology, to facial expression analysis, human action recognition, and video surveillance.

Walter N. Meier was born in Farmington, Michigan. He received a B.S. degree in aerospace engineering from the University of Michigan in 1991, a M.S. degree (in 1992) and a Ph.D. (in 1998) in aerospace engineering sciences from the University of Colorado, Boulder within the universitys interdisciplinary Program in Atmospheric and Oceanic Sciences.

He is currently a research scientist at the NASA Goddard Space Flight Center Cryospheric Sciences Lab in Greenbelt, Maryland, USA. Previously, he has worked as research scientist at the National Snow and Ice Data Center in Boulder, Colorado, as an adjunct assistant professor at the United States Naval Academy in Annapolis, Maryland, and as a visiting scientist at the United States National Ice Center in Washington, DC. Dr. Meier is a member of the American Geophysical Union.